Electronic band structures of the scheelite materials $CaMoO_4$, $CaWO_4$, $PbMoO_4$, and $PbWO_4$

Y. Zhang, N. A. W. Holzwarth, and R. T. Williams
Department of Physics, Wake Forest University, Winston-Salem, North Carolina 27109
(Received 6 January 1998)

Density-functional calculations using the linearized-augmented-plane-wave method were carried out for the scheelite materials $CaMoO_4$, $CaWO_4$, $PbMoO_4$, and $PbWO_4$ in order to determine their ground-state electronic properties. The results indicate that $CaMoO_4$ and $CaWO_4$ have direct band gaps at the center of the Brillouin zone, while $PbMoO_4$ and $PbWO_4$ have band extrema at wave vectors away from the zone center with possibly indirect band gaps. The magnitudes of the band gaps increase in the order $PbMoO_4 < PbWO_4 < CaMoO_4 < CaWO_4$. The valence and conduction bands near the band gap are dominated by molecular orbitals associated with the $MoO_4^{-\alpha}$ and $WO_4^{-\alpha}$ ions, where $\alpha \approx 2$. The valence-band widths are 5 and 5.5 eV for the Ca and Pb materials, respectively. In the Pb materials, the Pb $6s$ states form narrow bands 1 eV below the bottom of the valence bands, and also hybridize with states throughout the valence bands, while the Pb $6p$ states hybridize with states throughout the conduction bands. In the Ca materials, the Ca $3d$ states contribute to a high density of states 3–4 eV above the bottom of the conduction bands. [S0163-1829(98)10019-X]

I. INTRODUCTION

Calcium and lead molybdates and tungstates are naturally occurring minerals which can also be made synthetically, and which have very interesting luminescence and structural properties. The mineral names associated with these materials are powellite ($CaMoO_4$), scheelite ($CaWO_4$), wulfenite ($PbMoO_4$), and stolzite ($PbWO_4$). The name ''scheelite'' is also used to describe the common crystal structure of these materials. These materials have been very extensively studied during the past century. For example, a 1948 monograph by Kröger[1] presented a thorough summary of the luminescence properties of these and related materials and their solid solutions. Recently, $PbWO_4$ has attracted special interest because of plans to use it as a scintillator in detectors at the Large Hadron Collider in CERN.[2] There are still some very fundamental questions concerning the electronic properties of these materials, especially concerning the nature of the states of the ideal crystal in the vicinity of the band gap. In order to address some of these questions, we have calculated the self-consistent electronic structure of the four materials in the framework of density functional theory[3,4] using a relativistic linearized-augmented-plane-wave (LAPW) technique.[5,6]

The paper is organized as follows. In Sec. II the crystal structure is described. The calculational method is discussed in Sec. III. The results for the densities of states, the band structures, and the electron density distributions are presented in Sec. IV. In Sec. V the work is analyzed in terms of earlier theoretical and experimental work, and the main results are summarized.

II. CRYSTAL STRUCTURE

The scheelite crystal structure is characterized by the tetragonal space group $I4_1/a$ or C_{4h}^6 (listed as No. 88 in the Ref. 7). In this structure, the primitive unit cell has two ABO_4 units (where A = Ca or Pb and B = Mo or W). The A and B sites have S_4 point symmetry, and the crystal has an inversion center. The O sites have only a trivial point symmetry, and are arranged in approximately tetrahedral coordination about each B site. The crystal has three crystal parameters $\{x,y,z\}$ which describe the location of the O sites. There are a number of equivalent ways to describe the structure which have appeared in the literature.[8] Table I lists some representative values of the crystal parameters that have been determined by x-ray and neutron diffraction, with $\{x,y,z\}$ defined relative to the origin of the crystal at the inversion center and confined to the sector $0 < \{x,y\} < \frac{1}{2}$ and $0 < z < \frac{1}{8}$. The starred references indicate the values used in the present electronic structure calculations.

The crystal structure has been described[8] as highly ionic with $A^{+\alpha}$ cations and tetrahedral $BO_4^{-\alpha}$ anions, where $\alpha \approx 2$. The $BO_4^{-\alpha}$ anions are themselves highly ionic with formal charges of $B^{+\beta}$ and $O^{-\gamma}$, where $4\gamma - \beta \equiv \alpha$. If there were no covalent bonding, β and γ would take the values 6 and 2, respectively. The tetrahedral $BO_4^{-\alpha}$ anions have short B-O bond lengths ranging from 1.77 Å for $CaMoO_4$ to 1.79 Å for $PbWO_4$, which are quite rigid even under pressure.[9] Figure 1 shows a perspective drawing of the crystal structure of $PbWO_4$ in the conventional unit cell, indicating the a and c axes and the nearly tetrahedral bonds between O and W. Also included in this figure is a plane which passes through two W-O bonds and one of the Pb sites. A contour map of the valence-electron density which is indicated on this plane will be discussed further in Sec. IV.

III. CALCULATIONAL METHODS

The calculations reported in this paper were performed with the LAPW technique using the WIEN97 code.[6] The exchange-correlation functional was taken within the local-density approximation using the form developed by Perdew and Wang.[10] The calculational and convergence parameters used for all four materials are listed in Table II. The muffin-tin radii for O, Mo, and W were chosen to be slightly less than half the O-Mo and O-W bond lengths. For Pb, a muffin-tin radius of 1.9 bohr was chosen in order to avoid the numerical instabilities of ''ghost'' states. The plane-wave ex-

 © 1998 The American Physical Society

TABLE I. Some representative experimental data for ABO_4 scheelite crystals at room temperature. Quoted values refer to the conventional unit cell structure with A sites at $\pm(0,\frac{1}{4},\frac{5}{8})$, B sites at $\pm(0,\frac{1}{4},\frac{1}{8})$; and O sites at $\pm(x,y,z)$, $\pm(\frac{1}{2}-x,-y,\frac{1}{2}+z)$, $\pm(-\frac{1}{4}-y,\frac{1}{4}+x,\frac{1}{4}+z)$, and $\pm(-\frac{1}{4}+y,-\frac{1}{4}-x,-\frac{1}{4}+z)$, where 12 additional lattice sites are generated by adding $(\frac{1}{2},\frac{1}{2},\frac{1}{2})$. Some references use the alternative O site parameters $x\rightarrow\frac{1}{4}-y$, $y\rightarrow\frac{1}{4}-x$, and $z\rightarrow\frac{1}{4}-z$. Still other references choose the origin of the unit cell at the site of a B atom, with the corresponding O positions described with parameters $x\rightarrow x$, $y\rightarrow\frac{1}{4}-y$, and $z\rightarrow\frac{1}{8}-z$. The experimental methods are abbreviated with ''XP'' for x-ray powder, ''XC'' for x-ray single crystal, and ''N'' for neutron diffraction. The starred rows indicate the parameters used in the present calculations.

Material	Year	Refs.	Method	a (Å)	c (Å)	c/a	x	y	z
$CaMoO_4$	1943	8,39	XP	5.213	11.426	2.192	0.25	0.10	0.05
	1971	40	N	5.226	11.43	2.187	0.2428	0.1035	0.0424
	1972	41	XP	5.2256	11.434	2.188			
	*1985	9	XC	5.222	11.425	2.188	0.2431	0.1010	0.0411
$CaWO_4$	1943	8,39	XP	5.230	11.348	2.170	0.25	0.10	0.05
	1964	42	XC	5.234	11.376	2.170	0.2415	0.0996	0.0389
	1964	43	N				0.2413	0.0989	0.0389
	1972	44	XP	5.2437	11.3754	2.169			
	1972	41	XP	5.2419	11.376	2.170			
	*1985	9	XC	5.2429	11.3737	2.169	0.2414	0.0993	0.0394
	1989	45	XP	5.24294	11.373	2.169			
$PbMoO_4$	1943	8,39	XP	5.424	12.076	2.226	0.25	0.12	0.05
	*1965	46	N	5.4312	12.1065	2.229	0.2352	0.1143	0.0439
	1972	47	XP	5.4360	12.1107	2.228			
	1972	41	XP	5.4355	12.108	2.228			
	1985	9	XC	5.4351	12.1056	2.227			
$PbWO_4$	1943	8,39	XP	5.448	12.016	2.206	0.25	0.12	0.05
	1972	41	XP	5.4622	12.048	2.206			
	1985	9	XC	5.4595	12.0432	2.206			
	*1996	48	XC	5.456	12.020	2.203	0.2388	0.1141	0.0429
	1996	49	XC	5.4612	12.0452	2.206	0.2524	0.1364	0.0446

pansion cutoffs were chosen to be 6 bohr^{-1} for expanding the wave functions and 14 bohr^{-1} for expanding the densities and potentials. The **k**-point sampling was chosen to be six irreducible points within the Brillouin zone. For this choice of parameters, the bottleneck of the calculation is diagonalization of the plane-wave Hamiltonian matrices which have a dimension of roughly 5000. We estimate that the convergence error of the calculation is dominated by the plane-wave cutoff, and the total energy error is at most 0.2 eV. The **k**-point sampling error for the total energy is estimated to be at most 0.01 eV. Although, for structural optimization studies, the convergence parameters would have to be increased, the present choice of parameters ensures very good convergence of the one-electron energies, with estimated errors of at most 0.002 eV. In fact, for this choice of plane-wave cutoff parameters, nonrelativistic LAPW density-of-states results for $CaMoO_4$ were compared with the density of states determined from a completely independent calculational method—namely, the projector augmented wave (PAW) technique.[11,12] The two density-of-states plots were *virtually indistinguishable* over a 66-eV range of upper core, valence-band, conduction-band states, providing further evidence of the convergence of the one-electron energies.

Both scalar-relativistic and spin-orbit contributions were calculated self-consistently using the WIEN97 code.[6] In each self-consistency iteration, the scalar-relativistic Hamiltonian was diagonalized in the usual LAPW representation. The full relativistic Hamiltonian was then evaluated and diagonalized in the basis of the scalar-relativistic eigenstates, with the spin-orbit interaction approximated as a spherically symmetric contribution confined within each muffin-tin sphere. This approximation has been well studied, and has been shown to work well for elements in the fifth row of the Periodic Table.[5] It may, however cause greater errors for W and Pb which are in the sixth row of the Periodic Table.

IV. RESULTS

Density-functional theory[3,4] is designed to determine accurately the ground-state total energy and electron density of many-electron materials. The one-electron energies $E_{n\mathbf{k}}$ and their corresponding wave functions $\Psi_{n\mathbf{k}}(\mathbf{r})$ are variational parameters which are only qualitatively related to the measurable spectrum of the material. For example, although it is tempting to interpret the energy gap as the energy difference between the bottom of the first unoccupied band and the top of the last occupied band, density-functional theory is notorious for underestimating the measurable band gap of most materials. Nevertheless, by focusing on the comparison of the results for the four materials of this study we can obtain useful qualitative information about their ground-state properties.

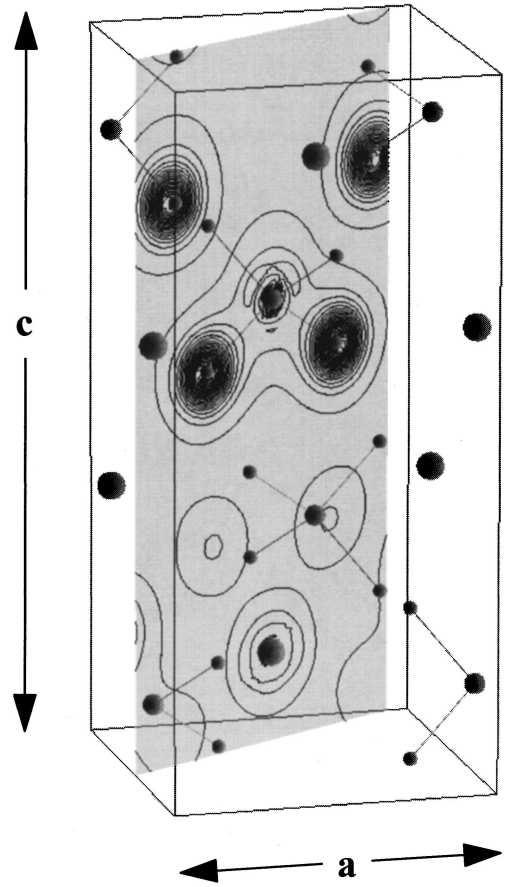

FIG. 1. Perspective drawing of the structure of $PbWO_4$ indicating the a and c axes. The atomic positions are indicated by spheres. The largest spheres (with no bonds) are the Pb sites; the middle size spheres at the W sites and the smallest spheres at the O sites are connected along nearest-neighbor bonds. The shaded plane passes through two W-O bonds and one of the Pb sites. Contour levels corresponding to the occupied electron density in the valence band are indicated on this plane with lowest contour level at $0.1e/\text{Å}^3$ and with a spacing of $0.25e/\text{Å}^3$ between contours.

A. Densities of states

The densities of states were calculated by approximating the δ function in energy with a Gaussian smearing function[13] of the form

$$N^x(E) \equiv \sum_{n\mathbf{k}} f^x_{n\mathbf{k}} w_{\mathbf{k}} \frac{e^{-(E-E_{n\mathbf{k}})^2/\sigma^2}}{\sqrt{\pi}\sigma}. \quad (1)$$

TABLE II. List of calculational and convergence parameters used for LAPW calculations.

Muffin-tin radii:	Ca, Pb	1.9 bohr
	Mo, W	1.65 bohr
	O	1.65 bohr
Maximum $\lvert\mathbf{k}+\mathbf{G}\rvert$ for wave functions		6 bohr^{-1}
Maximum $\lvert\mathbf{G}\rvert$ for charge density		14 bohr^{-1}
Inequivalent $\mathbf{k}$ points for BZ integrals		6
Convergence tolerance of total energy		0.001 eV

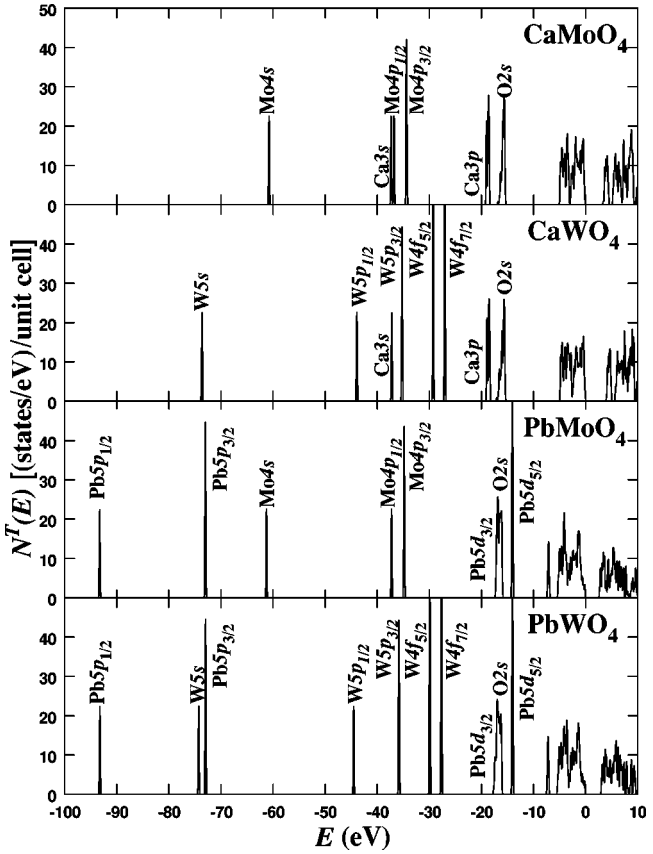

FIG. 2. Plot of total densities of states per unit cell for the four ABO_4 scheelite materials, evaluated using Eq. (1) with $\sigma = 0.1$ eV, including upper core, valence-band, and conduction-band states. The zero of energy is taken at the top of the last occupied states. The upper core states are labeled according to their dominant atomic behavior.

The Gaussian smearing parameter was chosen to be σ=0.1 eV. In Eq. (1), $w_{\mathbf{k}}$ is the Brillouin-zone sampling weight factor and $f^x_{n\mathbf{k}}$ is a weight factor associated with the state $n\mathbf{k}$. The six-$\mathbf{k}$-point sampling of the Brillouin zone did a good job of approximating the occupied densities of states. However, for states having larger dispersion such as in the upper portion of the conduction band, the approximation deteriorated somewhat. For the total density of states N^T, $f^T_{n\mathbf{k}}$ is equal to the degeneracy (including spin degeneracy) of the state. For the partial density of states N^a, $f^a_{n\mathbf{k}}$ is equal to the degeneracy multiplied by the fractional charge within the muffin-tin sphere a for the state. In addition to the total density of states, there are four interesting choices for partial densities of states that will be presented below.

Figure 2 compares the total densities of states (N^T) for the four compounds within a 110-eV range, with the zero of energy taken at the top of the last occupied band. The upper core states are labeled according to their dominant atomic character. The similarities in the electronic structure of the four materials is quite apparent from this figure. The one-electron energies of the upper core states including the Pb $5p_{1/2,3/2}$, Pb $5d_{3/2,5/2}$, W $5s$, W $5p_{1/2,3/2}$, W $4f_{5/2,7/2}$, Mo $4s$, Mo $4p_{1/2,3/2}$, Ca $3s$, Ca $3p$, and O $2s$ states have very small relative chemical shifts in these materials. The O $2s$ states are among the upper core states forming a narrow band having a width of about 2 eV. In the Pb materials, this O $2s$

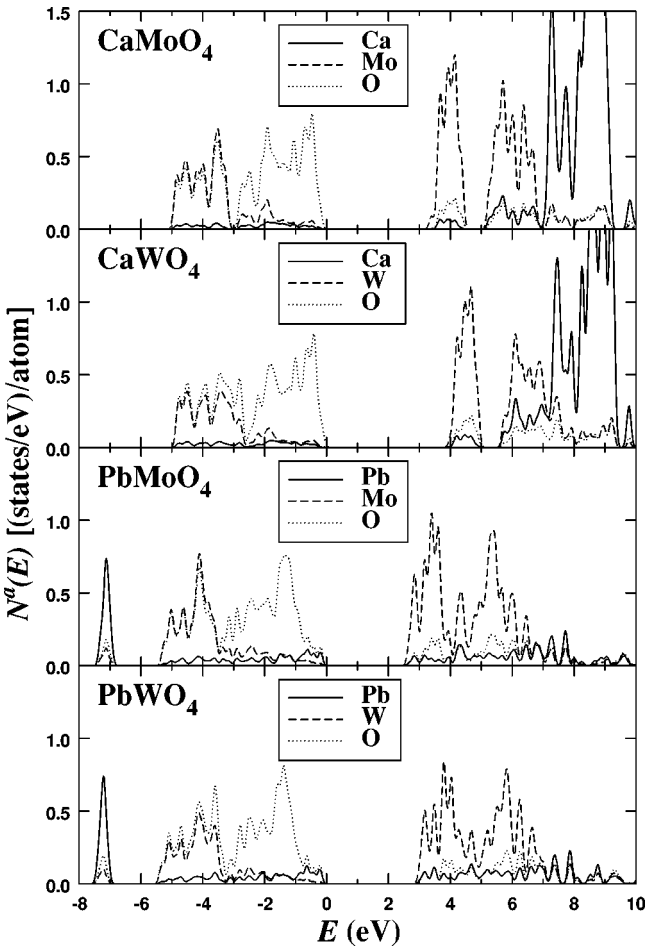

FIG. 3. Atomic partial densities of states per muffin-tin sphere for the four ABO_4 scheelite materials, evaluated as described in Fig. 2. The partial densities were weighted by the charges within a muffin-tin sphere for Ca or Pb (solid line), Mo or W (dashed line), and O (dotted line).

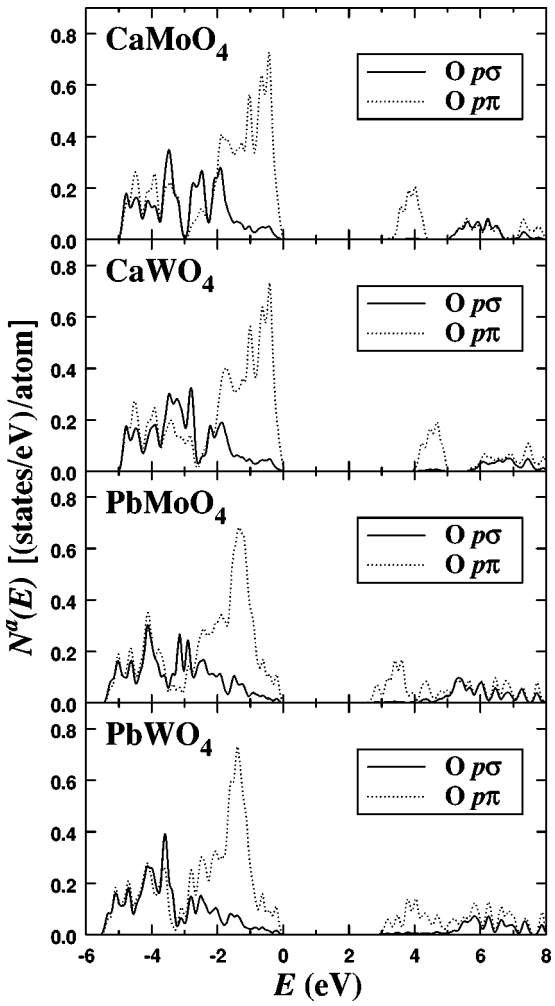

FIG. 4. Crystal-field-split O $2p$ partial densities of states per muffin-tin sphere for the four ABO_4 scheelite materials, evaluated as described in Fig. 2. The partial densities were weighted by the σ-like (full line) and π-like (dotted line) charges within each O muffin-tin sphere.

band peaks at -17 eV, and is degenerate with the Pb $5d_{3/2}$ states but separated from the very narrow Pb $5d_{5/2}$ band at -14 eV. In the Ca materials, the O $2s$ band peaks at -16 eV and is well separated from other core states of the system.

Partial densities are presented on expanded scales in Figs. 3, 4, 5, and 6. The muffin-tin sphere radii used to calculate the weight factors for the partial densities of states are listed in Table II. In general, these radii are much smaller than typical atomic radii for these atoms, and the total muffin-tin volume accounts for only 10–12 % of the volume of the crystal. Nevertheless, one can obtain qualitative information about the atomic origins of the valence- and conduction-band states of these materials.

The partial densities of states based on charge within each muffin-tin sphere (N^a for $a=$Ca, Pb, Mo, W, or O) are presented for the valence and conduction bands in Fig. 3. In $PbMoO_4$ and $PbWO_4$ there is a narrow Pb contribution to the density of states, having a width of 0.5 eV and centered at -7.1 and -7.2 eV, respectively, separated by more that 1 eV from the bottom of the main part of the valence bands. These bands, due to the Pb $6s$ states, accommodate four electrons per unit cell. Since the Pb $6s$ wave functions are so diffuse, there is significant mixing with O and Mo or W states, as will be discussed below. For all four materials, the main part of the valence bands accommodates 48 electrons per unit cell with a bandwidth of 5 eV for the calcium materials and 5.5 eV for the lead materials. The shape of the density of states for these valence bands has two main features. The lower portion of the bands has roughly equal contributions from O and Mo or W states per atom, while the upper portion contains states of primarily O character. If we had plotted the partial density of states per unit cell, the O contributions would be four times larger than the contributions from Ca, Pb, Mo, and W presented in Fig. 3. From this point of view, it is clear that O states dominate the character of these valence bands. In fact, these valence bands accommodate the same number of electrons per unit cell (48) as if they were filled with pure O $2p$ states. The bottom of the conduction bands of these materials is dominated by Mo and W states. The calcium materials have additional conduction-band contributions from the Ca states at approximately 3–4 eV above the bottom of the conduction band.

In order to investigate the nature of the valence and conduction bands further, we analyzed the partial densities in three additional ways—in terms of the $2p\sigma$ and $2p\pi$ contri-

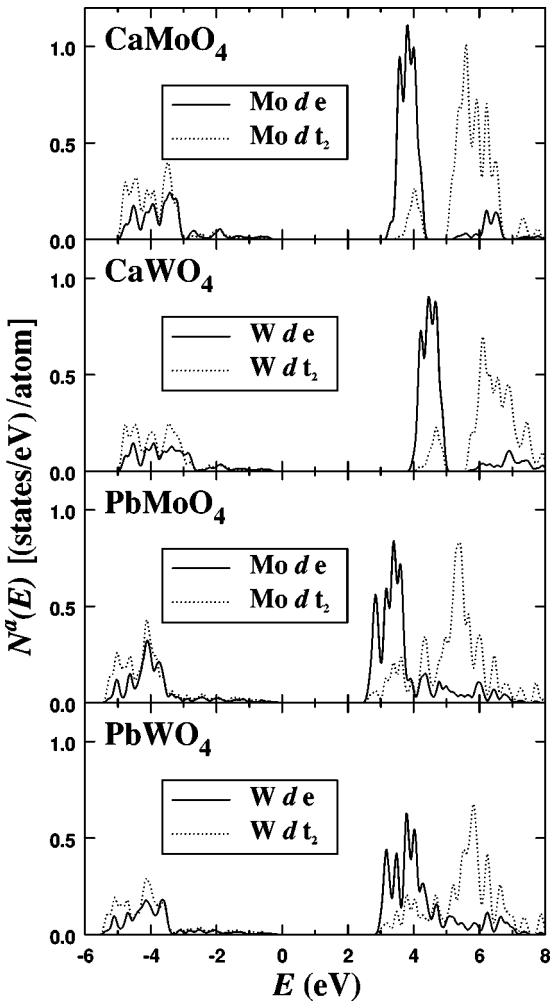

FIG. 5. Crystal-field-split $4d$ and $5d$ partial densities of states per muffin-tin sphere for the four ABO_4 scheelite materials, evaluated as described in Fig. 2. The partial densities were weighted by the e-like (full line) and t_2-like (dotted line) charges within a Mo or W muffin-tin sphere.

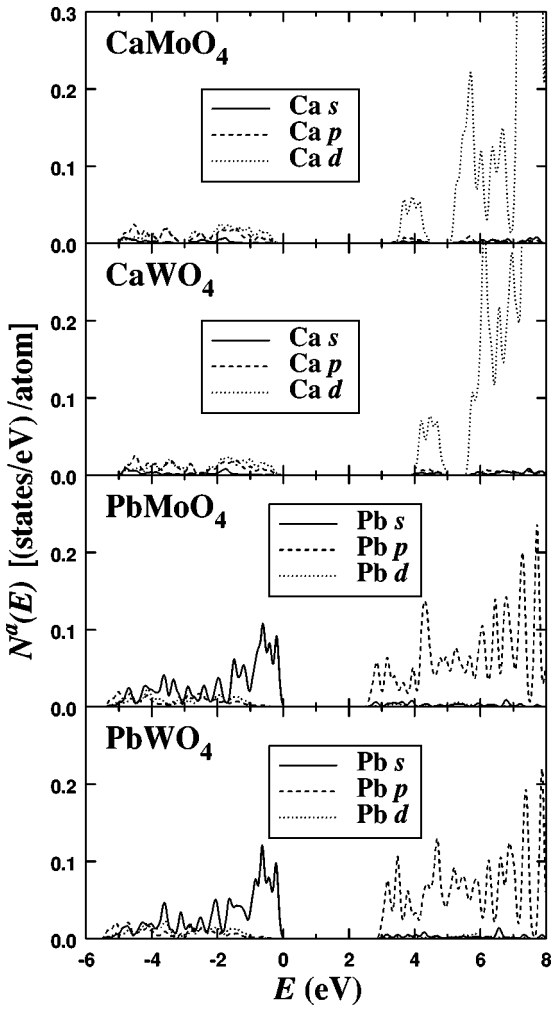

FIG. 6. Ca and Pb atomic-orbital partial densities of states for the four ABO_4 scheelite materials, evaluated as described in Fig. 2. The partial densities were weighted by the s-like (full line), p-like (dashed line), and d-like (dotted line) charges within each Ca or Pb muffin-tin sphere.

butions on the O sites (Fig. 4), the crystal-field-split $4d$ or $5d$ contributions on the Mo or W sites (Fig. 5), and in terms of the partial-wave composition of the Ca and Pb contributions (Fig. 6).

On the oxygen sites, the valence-band states are almost entirely described by atomiclike $2p$ wave functions. The strong crystal field due to the nearby Mo or W ions splits the atomic $2p$ states into σ and π contributions, as shown in the partial density-of-states plot of Fig. 4. From this figure, it is apparent that the σ-like contributions are weighted toward the bottom of the valence band and the top of the conduction band, while the π-like contributions are stronger at the top of the valence band and bottom of the conduction band.

The geometry in the vicinity of the Mo or W sites is approximately tetrahedral and the $4d$ or $5d$ states split into e- and t_2-like states. The corresponding partial densities of states are plotted in Fig. 5. From this result it is apparent that the bottom of the valence band receives roughly equal contributions from both the e- and t_2-like states, while the top of the valence band receives very little contribution from either symmetry. The bottom of the conduction band, however, is dominated by e-like contributions, while the upper conduction band is dominated by t_2-like contributions. Not included in this plot are the Mo $5s$ and $5p$ and W $6s$ and $6p$ contributions, since these were found to be negligible.

Finally, it is interesting to investigate the partial-wave distribution of the Ca and Pb contributions to the valence and conduction bands. Since these sites are 2.5 or 2.6 Å away from the nearest-neighbor O sites, the crystal-field splittings for these states are very small. The Ca $4s$-, $4p$-, and $3d$- and the Pb $6s$-, $6p$-, and d-like contributions are shown in Fig. 6. The vertical scale has been expanded relative to that used in the previous figures, in order to compensate for the small muffin tin used in the calculations. In fact, since the atomic or ionic wave functions corresponding to Ca $4s$ and $4p$ states and Pb $6s$ and $6p$ states are very diffuse, even a larger muffin-tin radius could not contain the majority of the charge associated with these states. This figure shows that there are very little Ca $4s$ and $4p$ contributions to the valence- and conduction-band states between -6 eV and $+8$ eV. However, there is a significant contribution of the Ca $3d$ states above the Mo $4d$ and W $5d$ conduction-band states. In the Pb materials, the corresponding Pb $5d$ states are filled, as discussed above, so that there is no appreciable d-like den-

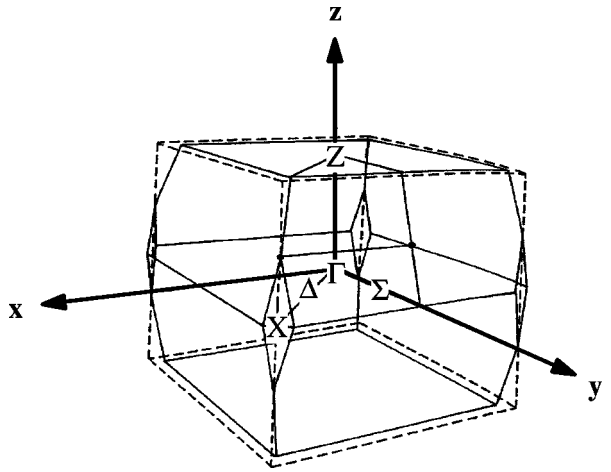

FIG. 7. Diagram of the Brillouin zone for a body-centered-tetragonal crystal structure, based on Ref. 38.

sity in the valence- and conduction-band region. Although the Pb $6s$ states form a well-defined narrow band below the bottom of the valence band, there is some additional Pb $6s$ character throughout the valence bands of $PbMoO_4$ and $PbWO_4$. Figure 6 also shows significant contribution of Pb $6p$ states throughout the conduction bands of these materials.

B. Electronic band-structure diagrams

Band dispersions for the four materials are plotted along three symmetry directions within the body-centered-tetragonal Brillouin zone (Fig. 7), and presented in Figs. 8 and 9. The shapes of the bands for $CaMoO_4$ and $CaWO_4$ are very similar to each other. The valence-band maxima and conduction-band minima are located at the Γ point, so that these are direct-gap materials. Although the values of the band gaps calculated within density-functional theory are known to be underestimated,[14] it is interesting to compare the gaps calculated for the two materials as listed in Table

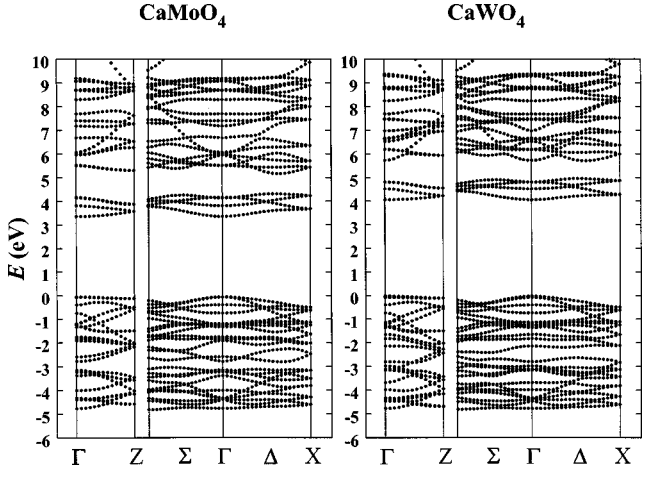

FIG. 8. Band-structure diagram for $CaMoO_4$ and $CaWO_4$ plotted in the range of 6 eV below and 10 eV above the valence-band maximum (taken as the zero of energy). The bands are plotted along the $\hat{\mathbf{z}}$ (c) axis from Γ to Z, and within the a plane from its boundary at $(\pi/a)[1+(a/c)^2]$ along the Σ direction to the Γ point and from the Γ point along the Δ direction to the X point, where the labels correspond to Fig. 7.

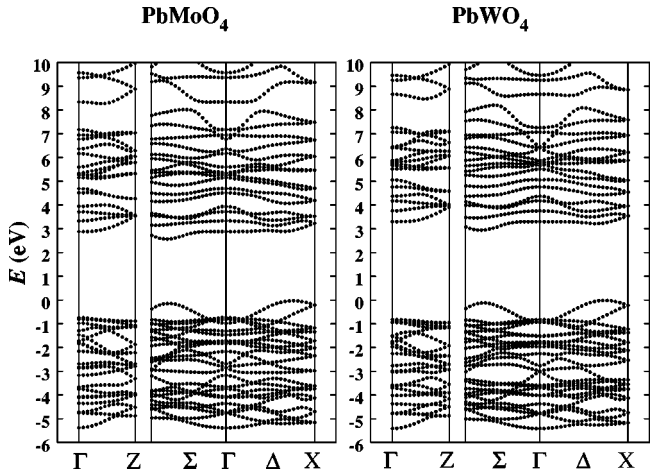

FIG. 9. Band-structure diagram for $PbMoO_4$ and $PbWO_4$ plotted in the same energy range, and along the same Brillouin-zone directions as in Fig. 8.

III. The dispersion of the valence bands is relatively small, with comparable dispersions along both the a and c directions. The lower part of the conduction band, which is composed primarily of e states associated with the Mo $4d$ or W $5d$ states, is separated by approximately 0.5 eV from the upper part of the conduction band formed from the t_2 states of Mo or W and the $3d$ states of Ca.

The shapes of the bands for $PbMoO_4$ and $PbWO_4$ are very similar to each other, but are somewhat different from those of the Ca materials. For the Pb materials, the band extrema are located away from the Γ point. Within the limited region of the Brillouin zone studied for the dispersion plot shown in Fig. 9, we can make the following statements about the band extrema. The valence band has maxima in the Δ directions, and slightly lower maxima in the Σ directions. The conduction-band minima are located in the Σ directions. The values of these indirect gaps are listed in Table III. The direct gaps for both materials appear to lie in the Σ direction, and are approximately 0.1 eV larger than the minimum (indirect) band gaps listed in Table III.

The calculated ordering of the band gaps is given by $PbMoO_4 < PbWO_4 < CaMoO_4 < CaWO_4$. Experimental data

TABLE III. Band gaps determined from the band dispersion calculations shown in Figs. 8 and 9 are listed for various values of $\mathbf{k}$ for the valence and conduction bands (k_v and k_c, respectively).

Material	E_{gap} (eV)	$k_v\left(\frac{2\pi}{a}\right)$	$k_c\left(\frac{2\pi}{a}\right)$
$CaWO_4$	4.09	Γ	Γ
$CaMoO_4$	3.41	Γ	Γ
$PbWO_4$	2.96	0.51 (Δ)	0.47 (Σ)
	3.06	0.47 (Σ)	0.47 (Σ)
	3.25	0.47 (Δ)	0.47 (Δ)
	4.13	Γ	Γ
$PbMoO_4$	2.59	0.57 (Δ)	0.47 (Σ)
	2.71	0.47 (Σ)	0.47 (Σ)
	2.93	0.51 (Δ)	0.51 (Δ)
	3.62	Γ	Γ

TABLE IV. Optical parameters (in units of eV) measured and deduced from experimental spectra. In a few cases, multiple entries are listed in order to illustrate the variability of these parameters, depending on temperature (T), sample preparation, and other factors.

	CaWO4	PbWO4	CaMoO4	PbMoO4
Luminescence peak ($E_{\rm lum}$)	2.9[a]	2.9[b]	2.3[a]	2.2[c]
Luminescence width (FWHM)	0.8[a]	0.8[b]	0.6[a]	0.6[c]
		0.7[b,d]		0.5[e]
Exciton reflectance peak ($E_{\rm exc}$)	5.9[f]	4.2[g,h]	5.0[f]	
Luminescence Stokes shift (ΔE_S)	3.0	1.3	2.7	
Free-carrier threshold ($E_{\rm fc}$)	7.0[i]	4.7[i]		
	6.5[j]			
	6.8[k]			
Exciton binding energy (E_b)	0.9	0.5		
Luminescence excitation threshold ($Y_{\rm th}$)	5.1[l]	4.1[g]	4.6[l]	3.4[c,e]
	4.7[m]	4.0[m]		

[a]Reference 50, $T=295$ K.
[b]Reference 51, $T=295$ K.
[c]Reference 31, 1.6 K$<T<$144 K.
[d]Reference 52, $T=4.2$ K.
[e]Reference 53, at $T=4.2$ K (luminescence spectrum); at $T=77$ K (excitation spectrum).
[f]Reference 22, $T=295$ K.
[g]Reference 24, $T=4.2$ and 295 K.
[h]Reference 23, $T=295$ K.
[i]Deduced from the thermoluminescence excitation spectra of Ref. 26, $T=80$ K.
[j]Reference 35, calcined powder sample, $T=295$ K.
[k]Reference 29, single crystal, $T=8$ K.
[l]Reference 54, $T=295$ K.
[m]Reference 26, $T=80$ K.

for exciton reflectance peak, luminescence excitation threshold, and free-carrier threshold summarized in Table IV are consistent with this ordering.

C. Electron-density distributions

In order to understand the electronic states of these materials further, we have constructed contour plots for their occupied and unoccupied states. Figure 1 shows a perspective diagram of a $PbWO_4$ crystal together with a plane which contains two W-O bonds and also contains a Pb site. A contour plot of the valence-electron density (including states within 5.5 eV of the valence-band maximum, but not the narrow Pb 6s band) is also indicated on this plane. Most of the contours shown in this diagram are associated with the four atoms in the plane, although there are significant contributions from two O's at the top of the diagram which lie in front or in back of the plane.

We have used the plane indicated in Fig. 1 to construct a series of contour diagrams for various partitions of the electronic charge densities of the four materials. Since the plots for $CaMoO_4$ and $CaWO_4$ and for $PbMoO_4$ and $PbWO_4$ look so similar to each other, we present only the plots for $CaMoO_4$ and $PbWO_4$. These contour plots all have the same uniform contour level spacing for all of the plots, namely, the contour levels are spaced at intervals of $0.2e/\text{Å}^3$, with the first contour level chosen to be $0.1e/\text{Å}^3$.

Figure 10 shows the electron density corresponding to the valence-band states of $PbWO_4$. The plot labeled (a) shows the contours corresponding to the narrow Pb 6s states below the valence band. With the exception of the small region of high density near the Pb site, most of the contours shown in the diagram correspond to oscillations about the $0.1e/\text{Å}^3$ level around the Pb site and near the O site. Plots labeled (b) and (c) correspond to the lower and upper portions of the

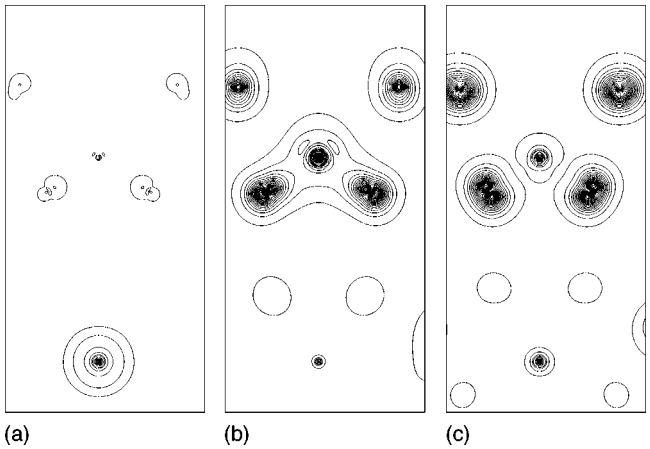

FIG. 10. Contour plot of the electronic charge density associated with the valence band of $PbWO_4$, showing separately the narrow 0.5-eV band associated with the Pb 6s states which is separated from the valence band by 1.5 eV (a), the bottom 2.3 eV of the valence bands (b), and the top 3.2 eV of the valence bands (c). The plane of the contour plot is the same plane as shown in Fig. 1, and passes through four atomic sites: two O sites, one W site, and one Pb site. The contour levels are uniformly spaced starting at $0.1e/\text{Å}^3$ with a spacing of $0.2e/\text{Å}^3$ between contours.

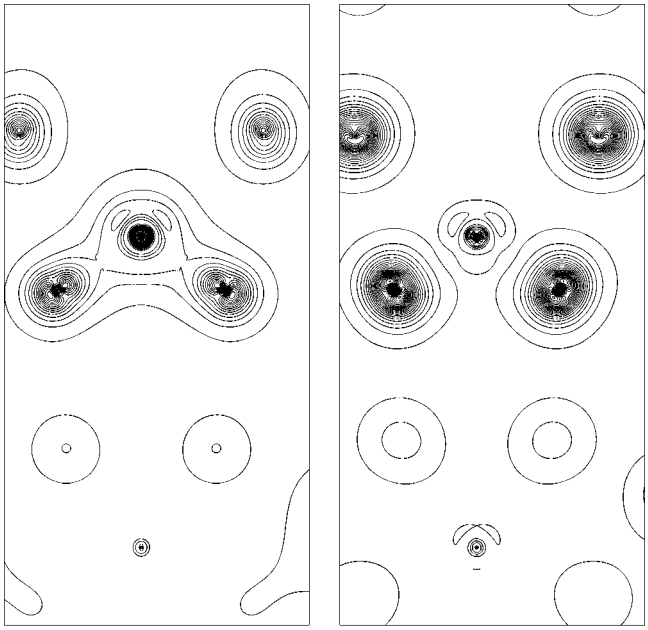

FIG. 11. Contour plot of the electronic charge density associated with the valence band of $CaMoO_4$, showing separately the bottom 1.9 eV (a) and the top 3.0 eV (b) portions. The plane of the contour plot and the contour levels are the same as in Fig. 10.

valence band, divided at the minimum in the density of states located 3.2 eV below the valence-band maximum. From these plots, it is evident that the lower bands (b) are dominated by σ bonding states formed from the O $2p$ and the W $5d$ states, while the upper bands (c) are dominated by π bonding states formed from the O $2p$ with somewhat less density associated with the W $5d$ states. This result is consistent with the density of states analysis discussed above. The sum of the densities (b) and (c) correspond to the density shown in the three-dimensional plot shown in Fig. 1.

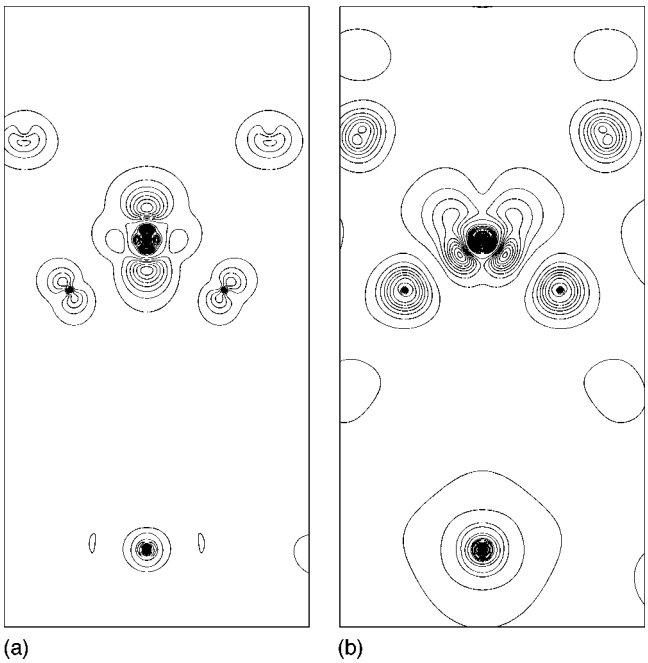

FIG. 12. Contour plot of the electronic charge density associated with the conduction bands of $PbWO_4$, showing separately the lower 2.1-eV portion (a) and the next higher 3.4-eV portion (b) of the conduction band. The plane of the contour plot and the contour levels are the same as in Fig. 10, with the density calculated from full occupancy of these states.

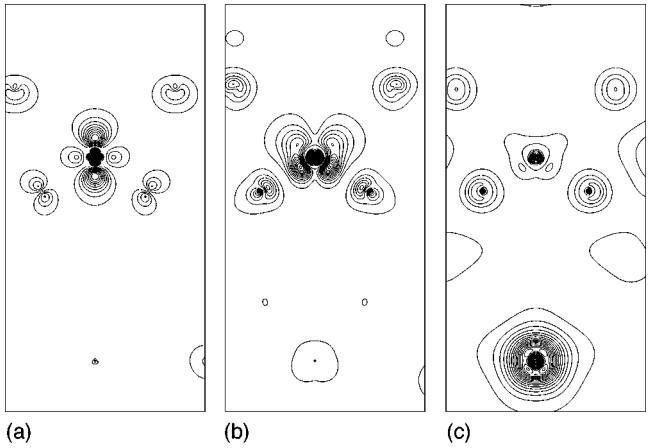

FIG. 13. Contour plot of the electronic charge density associated with the conduction bands of $CaMoO_4$, showing separately the lower conduction band having a width of 1.2 eV (a), the bottom 1.6 eV of the upper conduction band (which is 0.9 eV above the lower conduction band) (b), and the next 2.8 eV of the upper conduction band (c). The plane of the contour plot and the contour levels are the same as in Fig. 10, with the density calculated from full occupancy of these states.

Figure 11 shows the electron density corresponding to the valence-band states of $CaMoO_4$. Plots labeled (a) and (b) correspond to the lower and upper portions of the valence band, divided at the minimum in the density of states located 3.0 eV below the top of the valence-band maximum. These plots show very similar distributions to those of $PbWO_4$, showing the dominance of the O $2p\sigma$ states in the lower portion and the O $2p\pi$ states in the upper portion of the valence band.

Figures 12 and 13 show the electron density distributions in the unoccupied bands of $PbWO_4$ and $CaMoO_4$, respectively. The bottom portion of the conduction bands [labeled (a)] is dominated by states of e symmetry about the tetrahedral site formed from the W $5d$ or Mo $4d$ states with a small antibonding contribution from the O $2p\pi$ states. The upper portion of the conduction bands [labeled (b)] is dominated by states of t_2 symmetry formed from the W $5d$ or Mo $4d$ states with a small antibonding contribution from the O $2p\pi$ and $2p\sigma$ states. For $CaMoO_4$, the uppermost portion of the conduction band ($E>6.7$ eV) is plotted separately [labeled (c)], showing the contributions from the Ca $3d$ states.

V. DISCUSSION AND CONCLUSIONS

The results presented here represent an accurate self-consistent evaluation of the Schrödinger equation for the ground state of the system within the density-functional formalism. The total energy of the system and the corresponding electron density are determined variationally. However, the band structure and the corresponding densities of states are only qualitatively related to the ''quasiparticle'' states[14] which are accessible experimentally. Within this caveat, it is

useful to relate the present results to some of the experimental and theoretical results in the literature. For the purpose of the present qualitative discussion, we first relate our results to the ligand-field model used extensively in the literature, and then present a tentative comparison with some spectroscopic results.

A. Ligand-field model

For the purpose of this analysis, it is helpful to visualize the formation of these materials in the following way. Imagine that one could place the neutral atoms at the correct atomic positions in the crystal. First allow the neutral spherical atoms to self-consistently transfer charge to produce spherical $A^{+\alpha}$, $B^{+\beta}$, and $O^{-\gamma}$ ions as described in Sec. II. If the valence bands were formed only from O $2p$ states, the band filling would indicate that $\gamma=2$, $\beta=6$, and $\alpha=2$. Now apply degenerate perturbation theory to describe the splittings of the valence states of the spherical ions.[15] The splitting of the O $2p$ states is dominated by the Coulomb attraction of the electron to the nearest-neighbor $B^{+\beta}$ ion. The first order σ and π energy shifts are given, respectively, by

$$E^1_{p\sigma}=-\frac{2\beta e^2\langle r_p^2\rangle}{5R_{BO}^3} \quad \text{and} \quad E^1_{p\pi}=+\frac{\beta e^2\langle r_p^2\rangle}{5R_{BO}^3}. \tag{2}$$

Here R_{BO} is the Mo-O or W-O bond length, and $\langle r_p^2\rangle$ is the expectation value of the squared radius of the O $2p$ orbital. Using the estimated values of the parameters $\beta=6$, $R_{BO}=3.4$ bohr, and $\langle r_p^2\rangle=2$ bohr^2 (estimated from numerical integration using neutral O $2p$ wave functions), we find $E^1_{p\pi}-E^1_{p\sigma}\approx 5$ eV.

The splitting of the $4d$ or $5d$ states of the B ion is dominated by the Coulomb repulsion of the electron from the four tetrahedral nearest neighbor $O^{-\gamma}$ ions. The first-order energy shift for states of ''t_2'' and ''e'' symmetries are given, respectively, by

$$E^1_{t_2}=-\frac{8\gamma e^2\langle r_d^4\rangle}{27R_{BO}^5} \quad \text{and} \quad E^1_{e}=\frac{4\gamma e^2\langle r_d^4\rangle}{9R_{BO}^5}. \tag{3}$$

Here $\langle r_d^4\rangle$ is the expectation value of the fourth power of the radius of the d orbitals of the B ions. Using the estimated values of the parameters $\gamma=2$, $R_{BO}=3.4$ bohr, and $\langle r_d^4\rangle=9$ bohr^4 (the average value from numerical integration using Mo^{+6} $4d$ or W^{+6} $5d$ wave functions), we estimate $E^1_e-E^1_{t_2}\approx 1$ eV.

Finally, following the approach of Ballhausen and Liehr,[16] we allow the t_2 and e orbitals on the B sites to hybridize with linear combinations of $p\sigma$ and $p\pi$ ligand orbitals, symmetrized for the tetrahedral geometry, forming bonding and antibonding combinations which approximate the eigenstates of the $BO_4^{-\alpha}$ ions. The four ligand $p\sigma$ orbitals are compatible with the tetrahedral representation of symmetry a_1 and t_2, while the eight ligand $p\pi$ orbitals are compatible with the tetrahedral representation of symmetries t_1, t_2, and e. From our partial density-of-states analyses, we can roughly guess the ordering which would correspond to the molecular orbitals for the $BO_4^{-\alpha}$ clusters. These are shown in Fig. 14, where we have also indicated in the same diagram the positions of the atomiclike bands that we have identified in our calculations—Pb $6s$ states and Ca $3d$ states. This qualitative picture (apart from the ordering of the lower molecular-orbital states) is consistent with the early semiempirical molecular-orbital calculations for WO_4^{-2} and MoO_4^{-2} by several authors.[16–18] In particular, the early calculations recognized that the top occupied state has t_1 symmetry formed from the O $2p\pi$ states and the lowest unoccupied state has e symmetry formed from an antibonding combination of Mo $4d$ e or W $5d$ e state with O $2p\pi$ states. In fact, this model has been used more generally to describe the class of tetrahedral $BO_4^{-\alpha}$ anions.[19]

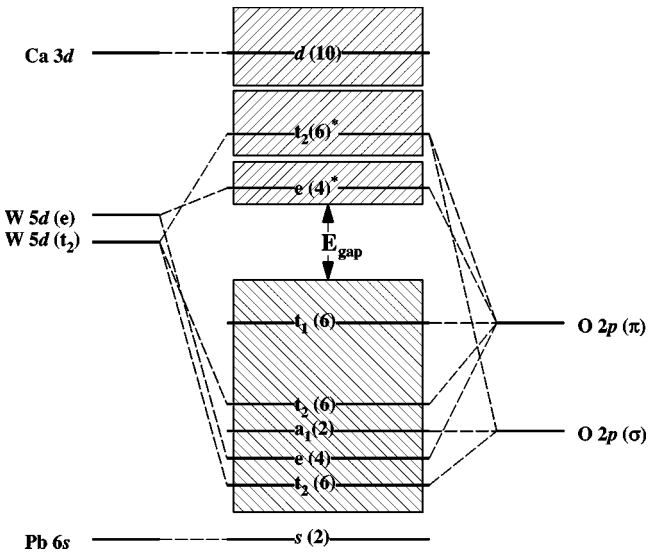

FIG. 14. Schematic diagram of the crystal-field splitting and hybridization of the molecular orbitals of a tetrahedral $WO_4^{-\alpha}$ (or $MoO_4^{-\alpha}$) cluster using the notation of Ref. 16, with ''*'' indicating anti-bonding (unoccupied) states. The numbers in parentheses indicate the degeneracy (including spin degeneracy) of each cluster state. The ordering of the molecular orbitals in the diagram approximates the partial density of states analyses. The shaded boxes are included to emphasize the fact that the discrete states are broadened by neighboring cluster interactions in the solid material. The relative positions of the Pb $6s$ states (for $PbWO_4$ and $PbMoO_4$) and Ca $3d$ states (for $CaWO_4$ and $CaMoO_4$) are also indicated on this diagram.

The fact that there is hybridization between the d orbitals of the $B^{+\beta}$ ions and the O $2p$ orbitals means that there is some covalent character to the bonding. From the ratio of occupied to unoccupied charge density within the muffin-tin spheres of the $B^{+\beta}$ ions, we estimate $\beta\approx 3$ for all four materials.

B. Comparison with optical spectra

A large portion of the interest in these materials is due to their intrinsic luminescence spectra.[1,2] While a detailed understanding of the luminescence processes goes far beyond the scope of the present study, we can make some qualitative comments. For each of the four materials, the intrinsic luminescence spectrum has been interpreted in terms of a molecular diagram such as Fig. 14, similar to that given by Ballhausen and Liehr.[16] The ground state of the system corresponds to filling all one-electron states below the band gap, resulting in a many-electron state of $^1A_1$ symmetry. The

lowest excited states involve one hole in the t_1 (primarily O $2p\pi$) states and one electron in the e (primarily Mo $4d$ or W $5d$) states, corresponding to the many-electron states $^1T_1$, $^3T_1$, $^1T_2$, and $^3T_2$. Of these states only the transition $^1A_1 \leftrightarrow {}^1T_2$ is a dipole-allowed transition. However, it is the lower $^3T_1$ or $^3T_2$ states which were shown to account for the intrinsic luminescence by a spin-forbidden transition to the ground $^1A_1$ state in optically detected electron paramagnetic resonance experiments on $CaMoO_4$ and $PbMoO_4$.[20,21]

While the molecular-orbital model describes the general features of the excitation and luminescence of these materials, a more accurate description corresponds to a Frenkel-type exciton[22–26] having energies within the band gap of the one-electron states.[27] Since the present study has calculated the one-electron states only, we have no detailed information about the excitons. However, having information about the band states, we can comment on the qualitative differences between the excitons in the Ca and Pb materials. In particular, several authors[23,25,26] have suggested that the Pb $6s$ and $6p$ states contribute in a significant way to the excitation and luminescence spectra of $PbWO_4$. One experimental impetus for this suggestion is that an exciton peak is found at considerably lower energy in $PbWO_4$ (4.2 eV) than in $CaWO_4$ (5.9 eV), despite the fact that both crystals have the same $WO_4^{-\alpha}$ complex anion and the same scheelite structure.

Thus Belsky *et al.* suggested that the first sharp reflectance peak in $PbWO_4$ at 4.17 eV is associated with Pb $6s \rightarrow 6p$ transitions.[23] In advance of an available band-structure calculation, they speculated that a narrow Pb^{+2} $6p$ subband at the bottom of the conduction band should be expected. However, the partial density-of-states $[N^a(E)]$ calculations presented in Figs. 3 and 6 do not exhibit a narrow Pb peak at the bottom of the conduction band nor at the top of the valence band. Rather, a nearly uniform density of Pb states is distributed throughout the conduction and valence bands. The only distinct narrow Pb $6s$ band is located *below* the valence bands. We will return later to a discussion of partial Pb character in the lowest exciton. Comparing second ionization potentials of Ca and Pb, Mürk *et al.* suggested another exciton model for $PbWO_4$ in which a hole residing mainly on the tungstate group is paired with an electron described as being in the Pb^+ state.[26]

The peak energies of intrinsic recombination luminescence in the four scheelite materials under consideration are listed in Table IV. The intrinsic luminescence energy $E_{\rm lum}$ is about 2.9 eV in both tungstates and about 2.3 eV in both molybdates, consistent with the view that the intrinsic luminescence mainly involves the tungstate (molybdate) complex anion. We have already seen that the exciton energy depends strongly on whether Ca or Pb is the cation. In contrast, the luminescence energy is almost independent of this factor.[28] The luminescence peaks are broad, having full width at half maximum (FWHM) around 0.7 eV at temperature $T = 295$ K. The intrinsic luminescence energy is Stokes shifted about 3 eV below the exciton reflectance peak in $CaWO_4$, and about 1.3 eV below the exciton in $PbWO_4$. Since the 2.9-eV luminescence in tungstates has been satisfactorily identified as intrinsic recombination luminescence, the large Stokes shift and broadband imply that excitons self-trap before emitting luminescence photons.[25,29,30] This conclusion is further supported by the Urbach slope parameter $\sigma_0 = 0.9$ measured for $PbMoO_4$ by Van Loo.[31] According to the theory of Refs. 32 and 33, $\sigma_0 < 1$ implies an exciton-phonon coupling constant strong enough to induce self-trapping. This has been confirmed by observations reported for a wide variety of crystals.[30] Because of the significant local lattice distortion that accompanies self-trapping, the states giving luminescence can be described reasonably well as molecular orbitals of the single distorted atomic group on which the exciton localizes. Van der Waals and co-workers used optically detected electron paramagnetic resonance to study the excited state responsible for the intrinsic green luminescence in $CaMoO_4$ (Ref. 20) and $PbMoO_4$.[21] The luminescence was found to originate from a spin triplet excited state localized on a MoO_4^{-2} ion distorted by a Jahn-Teller instability. In $PbWO_4$, the complex shape of the spectrum of the blue luminescence band was attributed by Polak *et al.*[34] to Jahn-Teller splitting of the nearly degenerate localized excited states of a WO_4^{-2} complex anion. In contrast, it is the delocalized exciton band states which determine the near-edge excitation spectrum.

The band gaps of $PbWO_4$ and $CaWO_4$ can be assigned on the basis of excitation spectra of thermoluminescence[26,29] or phosphorescence.[35] Excitation of thermoluminescence or trap-mediated recombination phosphorescence implies charge separation followed by capture in traps. Such excitation spectra may be considered to yield information similar to photoconductivity spectra, without the need to apply an external field. We have chosen the threshold for production of free carriers, $E_{\rm fc}$, as the beginning of the steep rising edge of the thermoluminescence excitation spectrum in $PbWO_4$ single crystals measured at 80 K by Mürk *et al.*[26] It is listed as $E_{\rm fc} = 4.7$ eV in Table IV. Estimating the free-carrier threshold for a single crystal of $CaWO_4$ at a roughly corresponding point on its thermoluminescence excitation spectrum,[26] we find $E_{\rm fc} \approx 7$ eV. Gurvich *et al.*[35] assigned $E_{\rm fc} \approx 6.5$ eV for calcined powder samples of $CaWO_4$ at 295 K, and Nagirnyi *et al.*[29] recently found $E_{\rm fc} \approx 6.8$ eV for single crystals of $CaWO_4$ at 8 K. We will adopt $E_{\rm fc} \approx 6.8$ eV as the band gap for data comparisons below.

We have made use of $E_{\rm fc}$ in order to overlay the valence-band density of states from the present calculation with spectra of reflectivity and luminescence excitation near the interband edge in $PbWO_4$ (Fig. 15) and in $CaWO_4$ (Fig. 16). Although it is not expected that optical spectra should be directly comparable to the valence band density of states in general, our rationale for the present comparison is that the main differences in band structure which we want to compare between $CaWO_4$ and $PbWO_4$ occur near the top of the valence band, whereas the conduction-band edge is similar in both materials. Furthermore, as long as we confine attention to transitions near the interband edge, overlapping optical transitions should not complicate the spectra so much as to obscure basic valence structure.

With these caveats in mind, we have aligned the top edge of the valence-band density of states, $N^T(E)$, with the photon energy $(h\nu)$ corresponding to the experimental band gap $E_{\rm fc}$, such that deeper valence states correspond to the higher photon energies needed to excite them. The implied assumption is that the important spectroscopic features near the interband edge represent mainly transitions from successively

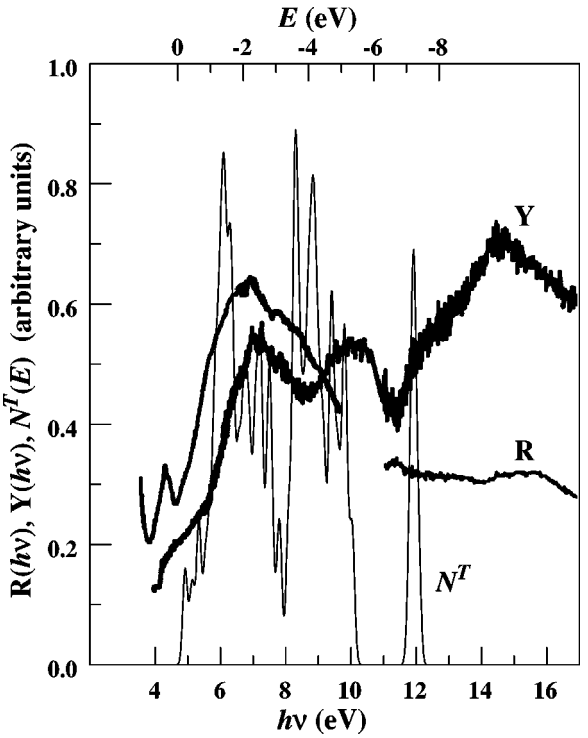

FIG. 15. Experimental spectra of reflectance $[R(h\nu)]$ and excitation yield of intrinsic luminescence $[Y(h\nu)]$ measured for $PbWO_4$ at liquid helium temperature in Ref. 24 are overlaid with the calculated total density of states $[N^T(E)]$. The experimental free-carrier excitation threshold $E_{fc}=4.7$ eV, as discussed in the text, is used to align the top ($E=0$ eV) of the valence density of states with the photon energy scale such that $h\nu$ is the energy from each plotted valence state to the conduction-band edge.

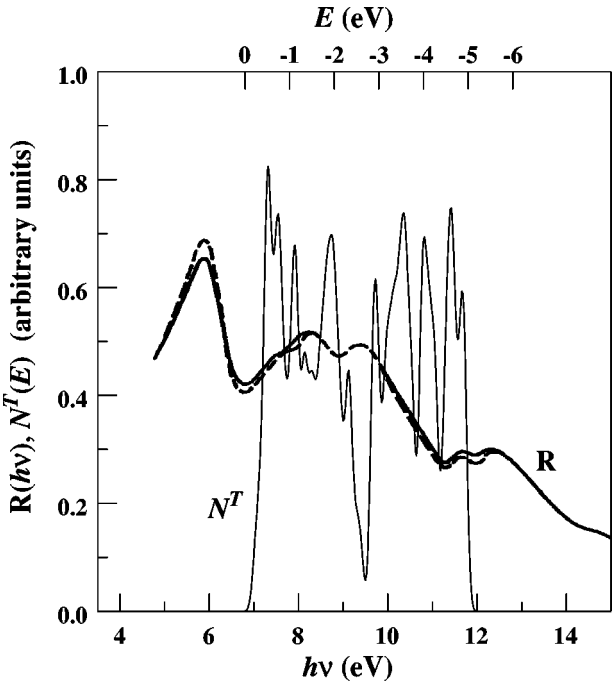

FIG. 16. Reflectance spectra $[R(h\nu)]$ measured for $CaWO_4$ in Ref. 22 are overlaid with the calculated total density of states $[N^T(E)]$. The broken and solid reflectance spectra were measured at 77 and 295 K, respectively. The experimental free-carrier excitation threshold $E_{fc}\approx 6.8$ eV, as discussed in the text, is used to align the top ($E=0$ eV) of the valence density of states with the photon energy scale, such that $h\nu$ is the energy from each plotted valence state to the conduction-band edge.

deeper valence states to just the conduction-band edge, and that a rough comparison to the density of initial states may be made without treating transition matrix elements explicitly. In future work, we will calculate optical constants from the band structure for a more accurate comparison over a larger photon energy range.

We focus now on the $PbWO_4$ reflectance and luminescence excitation spectra measured at liquid helium temperature by Kolabanov *et al.*[24] and reproduced in Fig. 15 with the aligned and overlaid valence-band density of states.[36] It is obvious that the lowest-energy peak in reflectivity lies within the band gap, in agreement with the previous identification of the 4.2-eV peak as an exciton.[22–26] The exciton binding energy is 0.5 eV if the band gap is $E_{fc}=4.7$ eV. The rise of reflectivity on the high-energy side of the exciton line coincides with the onset of interband transitions out of the highest valence states in the overlaid $N^T(E)$, starting at 4.7 eV on the photon energy scale. The luminescence excitation spectrum, which should have some correspondence to the absorption spectrum in this region, exhibits a shoulder roughly matching the shoulder at the top of the calculated valence $N^T(E)$. The strong O $2p$ peaks in the valence $N^T(E)$ spectrum rise sharply at about 6 eV on the aligned photon-energy scale, just where the experimental excitation spectrum turns sharply upward. The deeper group of valence bands accessible by photons above 8 eV seem a little misaligned with the valley at 8.6 eV and the peak at 10 eV in the excitation spectrum. This may indicate that we are getting too far from the interband edge for this simplistic comparison to valence structure to be faithful. Another reason for the apparent misalignment with the 10-eV peak in the excitation spectrum is that at least parts of the peaks at 10 and 15 eV probably correspond to excitation multiplication[37,29] at photon energies two and three times the band gap. We note that the isolated narrow Pb $6s$ peak in the calculated $N^T(E)$ at $h\nu=12$ eV ($E=-7.2$ eV) aligns well with the bump in the excitation spectrum at the corresponding energy.

Similar comparisons can be made for $CaWO_4$ reflectivity and the overlaid valence $N^T(E)$ in Fig. 16. With the band gap taken to be $E_{fc}\approx 6.8$ eV, as discussed above, the exciton reflectance peak at 5.9 eV implies a 0.9-eV binding energy of the exciton. Furthermore, we find reasonable qualitative correspondence between both the energy location and width of the valence $N^T(E)$ structure aligned in this way and the region of main reflectivity structure above the exciton, measured by Grasser *et al.*[22]

The shape of the optical spectra near the interband edge in $PbWO_4$ is suggestive of a weaker absorption threshold followed at higher energy by a stronger threshold in stair-step fashion, whereas in $CaWO_4$ there appears to be a main absorption threshold with which the exciton is associated. The ''strong'' absorption thresholds in both materials involve direct transitions at Γ starting from valence states with overwhelming O $2p$ character. The weaker threshold and associated exciton in $PbWO_4$ involve the topmost valence band, which disperses upward away from Γ, extending about 1 eV higher than the dominant O $2p$ bands at Γ. According to Fig. 9 and Table III, there is a minimum-energy direct transition

at about 0.5 along Σ, and another direct transition 0.19 eV higher at about 0.5 along Δ. In this regard, it is interesting to note that the 4.2-eV reflectance peak in $PbWO_4$ was resolved as a doublet with a 0.1 eV splitting at 4.2 K by Kolobanov *et al.*[24] An indirect gap from Σ to Δ lies about 0.1 eV lower in energy according to the present calculations. Since the exciton luminescence is emitted after self-trapping with 1.3-eV relaxation, luminescence spectra are unlikely to indicate whether an indirect edge lies 0.1 eV below the minimum direct edge. We know of no data yet available to support or rule out a minimum-energy indirect edge slightly below the direct edge.

We see in Fig. 3 that there is no peak in the partial density of states corresponding to Pb $6s$ orbitals $[N^{\mathrm{Pb}}(E)]$ at the energy of the topmost valence band. However, because $N^{\mathrm{O}}(E)$ dips sharply above the energy of the Γ critical point, the relative importance of the nearly constant $N^{\mathrm{Pb}}(E)$ increases significantly in the topmost band. With respect to some of the earlier discussions on the involvement of Pb states,[26,23,25] the topmost valence band may be described as having Pb $6s$ character with a strong admixture of O $2p$ character. Even though the distinct Pb $6s$ band actually lies below the valence bands at about -7.2 eV, we conclude that the presence of Pb (rather than Ca) in the $PbWO_4$ scheelite-type material also causes a band with hybrid Pb $6s$ and O $2p$ character to disperse upward from Γ and establish the minimum gap. However, a ''Pb $6s \rightarrow 6p$ exciton'' is not supported because no Pb^{+2} $6p$ discrete band was found at the bottom of the conduction band. The minimum-energy direct exciton in $PbWO_4$ should involve charge transfer from both lead and oxygen to mainly tungsten. In $CaWO_4$, and also in $PbWO_4$ at its second absorption threshold, the direct exciton at Γ involves charge transfer mainly from oxygen to tungsten.

C. Summary

For the four scheelite materials studied in this work, the results of the partial density-of-states analyses (Figs. 3, 4, 5, and 6) and electron-density contour plots (Figs. 10, 11, 12, and 13) together with the band-structure plots (Figs. 8 and 9) are in qualitative agreement with the energy-level diagram presented in Fig. 14. That is, the main features of the valence- and conduction-band states near the energy-band gap are well approximated by the molecular orbitals[16] of the tetrahedral molybdate or tungstate ions. The valence band accommodates 48 electrons per unit cell in one-to-one correspondence with the number of O $2p$ states. The shape of the valence-band density of states has two main peaks, with the upper peak primarily composed of O $2p\pi$ states and the lower peak composed of a combination of O $2p$ σ and π states together with contributions from the d states of Mo or W. The lowest conduction band is largely formed from e-symmetry states derived from d states of Mo or W and, in the Ca materials, is separated from the upper conduction band by a small gap. The upper conduction band is largely formed from t_2-symmetry states derived from d states of Mo or W. In the Pb materials, a narrow band of filled states is formed 1 eV below the valence bands as a result of the Pb $6s$ states. In the Ca materials, the $3d$ orbitals form a narrow band above the molybdate or tungstate conduction bands.

In addition to these general features, there is significant hybridization of the Pb $6s$ and $6p$ states throughout the valence and conduction bands of $PbMoO_4$ and $PbWO_4$, so that the band dispersions and splittings in the Pb materials are different from those of the Ca materials. In particular, the topmost valence band acquires significant Pb $6s$ character along with O $2p$ character, and disperses upward away from the Γ point of the Brillouin zone. We have analyzed some of the optical properties of these materials as summarized in Table IV, and made a rough comparison of our densities of states with reflectance and excitation yield data in Figs. 15 and 16. In the future, we hope to use the present results as a basis for a more thorough analysis of the optical properties of these materials.

ACKNOWLEDGMENTS

This project was supported by NSF Grant Nos. DMR-9403009, DMR-9706575, and DMR-9510297. We would like to thank Dimitri Alov for introducing us to the scheelite materials, for providing samples for the experimental work associated with this project, and for helpful discussions. We thank Martin Nikl and Vitali Nagirnyi for helpful comments on the manuscript, and also thank Eric Carlson, Abdessadek Lachgar, and Ekaterina Anokhina for symmetry and crystallographic advice, and Peter Blaha for help with the WIEN97 computer program.

[1] F. A. Kröger, *Some Aspects of the Luminescence of Solids* (Elsevier, New York, 1948).

[2] P. Lecoq, in *Proceedings of the International Conference on Inorganic Scintillators and Their Applications*, SCINT95, edited by Pieter Dorenbos and Carel W. E. van Eijk (Delft University Press, Delft, 1996), p. 52.

[3] P. Hohenberg and W. Kohn, Phys. Rev. **136**, B864 (1964).

[4] W. Kohn and L. J. Sham, Phys. Rev. **140**, A1133 (1965).

[5] David J. Singh, *Planewaves, Pseudopotentials and the LAPW Method* (Kluwer, Boston, 1994).

[6] P. Blaha, K. Schwarz, and J. Luitz, WIEN97, Vienna University of Technology, 1997 [Improved and updated Unix version of the original copyrighted WIEN code, which was published by P. Blaha, K. Schwarz, P. Sorantin, and S. B. Trickey, Comput. Phys. Commun. **59**, 399 (1990)].

[7] *International Tables for Crystallography*, edited by T. Hahn (Reidel, Boston, 1987), Vol. A.

[8] Lars Gunnar Sillén and Anna-Lisa Nylander, Ark. Kemi, Mineralogi Geologi **17A**, No. 4, 1 (1943).

[9] Robert M. Hazen, Larry W. Finger, and Joseph W. E. Mariathasan, J. Phys. Chem. Solids **46**, 253 (1985).

[10] John P. Perdew and Yue Wang, Phys. Rev. B **45**, 13 244 (1992).

[11] N. A. W. Holzwarth, G. E. Matthews, R. B. Dunning, A. R. Tackett, and Y. Zeng, Phys. Rev. B **55**, 2005 (1997); N. A. W. Holzwarth, G. E. Matthews, A. R. Tackett, and R. B. Dunning, *ibid.* **57**, 11 827 (1998).

[12] P. E. Blöchl, Phys. Rev. B **50**, 17 953 (1994).
[13] C. L. Fu and K. M. Ho, Phys. Rev. B **28**, 5480 (1983).
[14] Mark S. Hybertsen and Steven G. Louie, Comments Condens. Matter Phys. **13**, 223 (1987).
[15] Carl J. Ballhausen, *Introduction to Ligand Field Theory* (McGraw-Hill, New York, 1962).
[16] C. J. Ballhausen and Andrew D. Liehr, J. Mol. Spectrosc. **2**, 342 (1958).
[17] J. P. Dahl and C. J. Ballhausen, Adv. Quantum Chem. **4**, 170 (1968).
[18] R. Kebabcioglu and A. Müller, Chem. Phys. Lett. **8**, 59 (1971).
[19] S. P. McGlynn, T. Azumi, and D. Kumar, Chem. Rev. **81**, 475 (1981).
[20] W. Barendswaard and J. H. van der Waals, Mol. Phys. **59**, 337 (1986).
[21] J. Van Tol and J. H. van der Waals, Mol. Phys. **88**, 803 (1996).
[22] R. Grasser, E. Pitt, A. Scharmann, and G. Zimmerer, Phys. Status Solidi B **69**, 359 (1975).
[23] A. N. Belsky, V. V. Mikhailin, A. N. Vasil'ev, I. Dafinei, P. Lecoq, C. Pedrini, P. Chevallier, P. Dhez, and P. Martin, Chem. Phys. Lett. **243**, 552 (1995); A. N. Belsky, S. M. Klimov, V. V. Mikhailin, A. N. Vasil'ev, E. Auffray, P. Lecoq, C. Pedrini, M. V. Korzhik, A. N. Annenkov, P. Chevallier, P. Martin, and J. C. Krupa, Chem. Phys. Lett. **277**, 65 (1997).
[24] V. Kolobanov, J. Becker, M. Runne, A. Schroeder, G. Zimmerer, V. Mikhailin, P. Orekhanov, I. Shpinkov, P. Denes, D. Renker, B. Red'kin, N. Klassen, and S. Shmurak, in *Proceedings of the International Conference on Inorganic Scintillators and Their Applications*, SCINT95 (Ref. 2), pp. 249–251.
[25] S. G. Nedel'ko, A. S. Voloshinovshii, M. O. Krisjuk, Z. T. Moroz, and M. V. Pashkovskii, in *Proceedings of the International Conference on Inorganic Scintillators and Their Applications*, SCINT95 (Ref. 2), pp. 263–266.
[26] V. Mürk, M. Nikl, E. Mihoková, and K. Nitsch, J. Phys.: Condens. Matter **9**, 249 (1997).
[27] Robert S. Knox, *Theory of Excitons* (Academic, New York, 1963).
[28] Although the energy of luminescence depends little on the presence of Pb or Ca, the more detailed results available from electron paramagnetic resonance studies for several scheelite-structure molybdate crystals (Refs. 21 and 20) show that zero-field splitting and other respects are different when Pb replaces Ca or Cd. This was attributed qualitatively to the presence of the Pb^{+2} 6*s* electrons, which ''interact with the oxygen orbitals of the molybdate group and become involved in the excited states'' (Ref. 21).
[29] V. Nagirnyi, E. Feldbach, L. Jösson, M. Kirm, A. Lushchik, Ch. Lushchik, L. L. Nagornaya, V. D. Ryzhikov, F. Savikhin, G. Svensson, and I. A. Tupitsina, in *3rd International Symposium ''Luminescent Detectors and Transformers of Ionizing Radiation'' LUMDETR'97, October 1997, Ustron, Poland* [Radiat. Meas. (to be published)].
[30] K. S. Song and R. T. Williams, *Self-Trapped Excitons*, 2nd ed. *Springer Series in Solid-State Sciences*, Vol. 105 (Springer-Verlag, Berlin, 1996).
[31] W. Van Loo, Phys. Status Solidi A **27**, 565 (1975).
[32] Y. Toyozawa, Technical Report No. A119, ISSP, 1964 (unpublished).
[33] Michael Schreiber and Yutaka Toyozawa, J. Phys. Soc. Jpn. **51**, 1544 (1982).
[34] K. Polak, M. Nikl, K. Nitsch, M. Kobayashi, M. Ishii, Y. Usuki, and O. Jarolimek, J. Lumin. **72–74**, 781 (1997).
[35] A. M. Gurvich, É. R. Il'mas, T. I. Savikhina, and M. I. Tombak, J. Appl. Spectrosc. **14**, 751 (1973), originally published in Zh. Prikl. Spektrosk. **14**, 1027 (1971).
[36] Reflectance spectra from Refs. 24 and 23 are in basic agreement on the photon energies of the lowest exciton peak and most other near-edge features, but differ in the relative magnitude of reflectance at the exciton peak vs the interband region above it. We have chosen the data of Ref. 24 for comparison to the calculated $N^T(E)$ in Fig. 15, mainly because it also includes a luminescence excitation spectrum. Recently we became aware of new reflectivity and luminescence excitation spectra: I. A. Kamenskikh, V.N. Kolobanov, V. V. Mikhailin, I. N. Shpinkov, A. N. Vasil'ev, M. Kirm, and G. Zimmerer, DESY Annual Report, HASYLAB 1997 Annual Report, Part I, 1997, p. 252–253.
[37] A. Lushchik, E. Feldbach, R. Kink, Ch. Lushchik, M. Kirm, and I. Martinson, Phys. Rev. B **53**, 5379 (1996).
[38] Hiroshi Yamagami and Akira Hasegawa, J. Phys. Soc. Jpn. **61**, 2388 (1992).
[39] Lattice constants determined from x-ray powder data; oxygen positions determined from geometrical analysis of data in the literature.
[40] Erdogan Gürmen, Eugene Daniels, and J. S. King, J. Chem. Phys. **55**, 1093 (1971).
[41] A. W. Sleight, Acta Crystallogr., Sect. B: Struct. Crystallogr. Cryst. Chem. **28**, 2899 (1972).
[42] Allan Zalkin and David H. Templeton, J. Chem. Phys. **40**, 501 (1964).
[43] M. I. Kay, B. C. Frazer, and I. Almodovar, J. Chem. Phys. **40**, 504 (1964).
[44] V. T. Deshpande and S. V. Suryanarayana, J. Mater. Sci. **7**, 255 (1972).
[45] Frank N. Blanchard, Power Diff. **4**, 220 (1989).
[46] Janusz Leciejewicz, Z. Kristallogr. **121**, 158 (1965).
[47] S. V. Suryanarayana and V. T. Deshpande, Curr. Sci. **41**, 837 (1972).
[48] J. M. Moreau, Ph. Galez, J. P. Peigneux, and M. V. Korzhik, J. Alloys Compd. **238**, 46 (1996).
[49] Dimitri Alov (private communication).
[50] Nobuhiro Saito, Noriyuki Sonoyama, and Tadayoshi Sakata, Bull. Chem. Soc. Jpn. **69**, 2191 (1996).
[51] Masaaki Kobayashi, Mitsuru Ishii, Yoshiyuki Usuki, and Hiroshi Yahagi, Nucl. Instrum. Methods Phys. Res. A **333**, 429 (1993).
[52] M. Nikl, K. Nitsch, K. Polak, E. Mihokova, I. Dafinei, E. Auffray, P. Lecoq, P. Reiche, R. Uecker, and G. P. Pazzi, Phys. Status Solidi B **195**, 311 (1996).
[53] J. A. Groenink and G. Blasse, J. Solid State Chem. **32**, 9 (1980).
[54] William R. Hemphill, R. Michael Tyson, and Arnold F. Theisen, Economic Geol. **83**, 637 (1988).